Article:
Hua, Y, Shamsa, A, Barker, R orcid.org/0000-0002-5106-6929 et al. (1 more author) (2018) Protectiveness, morphology and composition of corrosion products formed on carbon steel in the presence of Cl^-, Ca^{2+} and Mg^{2+} in high pressure CO_2 environments. Applied Surface Science, 455. pp. 667-682. ISSN 0169-4332

https://doi.org/10.1016/j.apsusc.2018.05.140

Protectiveness, morphology and composition of corrosion products formed on carbon steel in the presence of Cl^-, Ca^{2+} and Mg^{2+} in high pressure CO_2 environments

Yong Hua*, Amir Shamsa, Richard Barker and Anne Neville
Institute of Functional Surfaces
School of Mechanical Engineering
University of Leeds
Leeds
LS2 9JT
United Kingdom
*Corresponding author: Yong Hua, Tel: 07923359918, Email: leo.huayong@gmail.com

Abstract

This study investigates the individual effects of chloride (Cl^-), calcium (Ca^{2+}), and magnesium (Mg^{2+}) ions on the CO_2 corrosion behaviour of carbon steel in simulated CO_2 geologic storage environments (60°C and 100 bar CO_2). The influence of the aforementioned ions was assessed over immersion times from 6 to 96 hours. The corrosion product growth was monitored over this period and related to the extent of both general and localised corrosion. For each test, corrosion product morphology and chemistry were analysed using a combination of scanning electron microscopy (SEM), focused ion beam (FIB) method, energy-dispersive X-ray spectroscopy (EDX) and X-ray diffraction (XRD).

Key words: CO_2 corrosion, supercritical, $FeCO_3$, $Fe_xCa_yCO_3$, $Fe_xMg_yCO_3$

1. Introduction

As part of the carbon capture and storage process, carbon dioxide (CO_2) is injected into either depleted hydrocarbon reservoirs, or saline aquifers for the purposes of geological storage[1]. Such formations consist of porous rock which, in the case of a saline aquifer, is filled with brine and can contain high concentrations of dissolved salts.

The pipelines facilitating the injection process receive CO_2, which descends the vertical injection line and is compressed by its own weight, resulting in the fluid being heated. At the point of injection, CO_2 is generally in a liquid or supercritical state.[2] For the selection of appropriate pipeline injection materials, two key types of corrosive environment should be considered. When continuous injection of CO_2 is performed, water is displaced from the head

of the injection pipeline. If this process is interrupted, brine will proceed to flow back to the injection point, potentially rising hundreds of meters before equilibrium is re-established.[2] Consequently, the injection line can be exposed to either a saline solution saturated with supercritical CO_2, or a supercritical CO_2 stream containing dissolved water. The second scenario is analogous to dense phase CO_2 pipeline transportation. However, it is the former scenario which is the focus of this study.

Despite its low corrosion resistance in CO_2-containing environments, carbon steel still remains the most commonly used pipeline material based on its widespread availability and low cost. The CO_2 corrosion mechanism involves a complex combination of chemical, electrochemical and transport processes. In addition to these, deposition or precipitation processes occur which result in the formation of corrosion products or mineral scales on the steel surface which can influence the corrosion mechanism. Typically, in 'simple' CO_2-saturated solutions with distilled water or only sodium chloride (NaCl) present as the dissolved salt, iron carbonate ($FeCO_3$) is the most commonly observed corrosion product.[3, 4] The importance of the formation of this crystalline layer has been well documented. It has been shown to block active sites on carbon steel surfaces, and act as a diffusion barrier to electrochemically active species, resulting in a significant reduction in steel corrosion rate under certain conditions.[5, 6, 7, 8, 9, 10, 11] In some instances in purely NaCl-containing CO_2-saturated brines, the formation of $FeCO_3$ has been shown to reduce the general corrosion rate of carbon steel by over an order of magnitude.[8, 12]

The structural and protective properties of the $FeCO_3$ layer have been shown to be highly dependent upon the concentration/activities of ionic species, temperature, pH and CO_2 partial pressure of the system in question.[13, 14] However, one potentially influential aspect which has received less attention is that of the brine chemistry and the effect of cations such as calcium (Ca^{2+}) and magnesium (Mg^{2+}). The presence of divalent salts can reduce CO_2 solubility and result in the precipitation of mineral scales such as calcium carbonate ($CaCO_3$) in the case of Ca^{2+} presence and magnesium carbonate ($MgCO_3$) in the case of Mg^{2+} presence. These mineral scales are different to $FeCO_3$ as the Fe^{2+} cation is produced predominantly as a result the corrosion process, whereas Ca^{2+} and Mg^{2+} exist within the formation.

Despite Mg^{2+} and Ca^{2+} salts being commonly found in the fluids of geological formations, their role on corrosion product formation on steel surfaces as well as their morphology, structure

and chemical properties, particularly in supercritical CO_2 conditions has received minimal research attention. This may be partly attributed to the fact that $CaCO_3$ and $MgCO_3$ are regarded as mineral scales and dealt with separately from $FeCO_3$, which is classified as a corrosion product. Regardless, very few studies have considered both mineral scaling and corrosion collectively in one system, despite both processes occurring simultaneously in many oil and gas as well as CO_2 injection scenarios.

2. *CO_2 corrosion research involving brine solutions containing Ca^{2+} and Mg^{2+}*

Limited research has focused on the effect of Ca^{2+} and Mg^{2+} on CO_2 corrosion of carbon steel, with most research directed towards NaCl solutions despite more complex brine chemistries existing in the field. A number of divalent cations are able to form carbonate scales/corrosion products on carbon steel surfaces, enabling them to drastically alter the corrosion mechanism. Both Ca^{2+} and Mg^{2+} tend to be two of the most abundant cations present within production fluid. These two ions have the ability to influence the CO_2 corrosion mechanism significantly given that the crystalline structure of $CaCO_3$ (specifically calcite) and $MgCO_3$ are similar to $FeCO_3$.

Due to the isostructurality of each of the aforementioned carbonates, Ca^{2+} and Mg^{2+} are able to substitute themselves for Fe^{2+} in the $FeCO_3$ structure, potentially leading to a change in the layer morphology and protectivesness. Literature relating to the role of such cations on the CO_2 corrosion mechanism is not only limited, but appears contradictory in nature, as will be discussed in the following paragraphs.

Shannon and co-workers[15] were perhaps the first researchers to establish that solution chemistry plays a key role in the protective characteristics of $FeCO_3$ in the 1970's, identifying that Mg^{2+} ions may be capable of improving both the protection and adhesion of $FeCO_3$. In a more recent study, Ingham et al.[16] used *in situ* synchrotron radiation X-ray diffraction (SR-XRD) to follow the formation of $FeCO_3$ at 80°C, 1 bar total pressure and pH 6.3. They suggested that the addition of magnesium chloride ($MgCl_2$) accelerated $FeCO_3$ precipitation, although these tests were performed using either a potentiostatic or galvanostatic method, producing anodic currents in excess of 10 mA/cm^2. Ingham et al. claimed that $MgCl_2$ (added as 0.02, 0.05 or 0.1M within a 0.5M NaCl solution) decreased the critical supersaturation required for precipitation, and also promoted the formation of chukanovite ($Fe_2(OH)_2CO_3$) in conjunction

with, but following $FeCO_3$ formation. Although traces of Mg were identified within the corrosion product layer in tests with the addition of 0.1M $MgCl_2$, there was no evidence to suggest that Mg had incorporated or was present in the formed corrosion product.

Zhao et al.,[17] performed experiments over 72 hours in the presence of Ca^{2+} and Mg^{2+} to evaluate the susceptibility of P110 steel to corrosion at 25 bar and 90°C. Their findings from potentiodynamic polarisation studies indicated that the combined presence of Ca^{2+} (6000 ppm) and Mg^{2+} (1,000 ppm) increase the anodic currents and decrease the cathodic currents. The addition of cations changed the corrosion product morphology and composition, with the layer being described as $Fe(Ca,Mg)(CO_3)_2$ in the presence of both cations.

Ding et al.[18] studied the corrosion behaviour of carbon steel exposed to simulated stratum water containing different Ca^{2+} concentrations at 10 bar and 75°C. Their results showed that the corrosion rate increased with increasing Ca^{2+} concentration from 256 to 512 mg/L. They found that $Fe_xCa_{1-x}CO_3$ formed on the sample surface and the Fe^{2+} in $FeCO_3$ was gradually replaced by more Ca^{2+} as the Ca^{2+} content increased in the solution. This was determined based on X-ray diffraction (XRD) patterns which resulted in a shift in $FeCO_3$ peak positions with increasing Ca^{2+} content. The observed shift is a result of the change in the unit cell of the corrosion products with the precipitation of $Fe_xCa_{1-x}CO_3$, as will be discussed later. In tests where both 512 ppm Ca^{2+} and 78 ppm Mg^{2+} were added to the brine, no Mg was observed in the corrosion product.[18].

In terms of the effects of Ca^{2+} addition on localised/pitting corrosion, Jiang et al.[19] performed corrosion experiments in 3 wt.% NaCl, 3 wt.% NaCl + 1.5% $CaCl_2$ and 4.6 wt.% NaCl with N80 steel at 57°C. Under static conditions, they found the corrosion rate increased with the rise in Cl^- concentration from 3 to 4.6 wt.% NaCl solution. In addition, they suggested that Cl^- was responsible for pitting and that Ca^{2+} played a role in delaying the initiation time of pits. Research by Ren et al.[20] also observed higher pitting rates for experiments on carbon steel with brines containing calcium chloride ($CaCl_2$) performed at 7 MPa and 80°C. They also ascribed the pitting behaviour to the presence of Cl^- ions.

Gao et al.[21] performed autoclave experiments in static and dynamic CO_2-saturated conditions with a brine containing 64 ppm Ca^{2+} and 78 ppm Mg^{2+}. Experiments were performed at different CO_2 partial pressures of 0.1, 0.3 and 1 MPa. In static experiments at

0.1 MPa CO_2, the corrosion product/scale consisted of separate $FeCO_3$, $MgCO_3$ and $CaCO_3$ phases. However, increasing partial pressure to 0.3 and 1 MPa resulted in the formation of $(Fe,Mg,Ca)CO_3$ and $(Fe,Ca)CO_3$, respectively. Under dynamic conditions, the composition of the scale was $(Fe,Ca)CO_3$, with no evidence of Mg presence within the corrosion product layer.

Tavares et al.[22] performed 28 day experiments to look at the effects of solid $CaCO_3$ addition to brine solutions on the corrosion rate of carbon steel at 80°C and 15 MPa in a CO_2-saturated 6.4M NaCl solution. 0.5M of $CaCO_3$ was added to the test solution, which was 10 times the mineral saturation limit. Tavares et al. reported that the addition of $CaCO_3$ reduced the corrosion rate of carbon steel, although this may have been attributed to the fact that $CaCO_3$ addition increased the solution pH from 2.71 to 4.7. For the $CaCO_3$-containing solution, the corrosion product produced on the surface was shown to exist as $Fe_xCa_{1-x}CO_3$ compared to $FeCO_3$ in the absence of $CaCO_3$. The Ca-containing layer was shown to be more porous and it was suggested that this made the steel surface more susceptible to Cl^- penetration, and as a result, pitting.

In more recent work, Esmaeely et al.[14] considered the effect of Ca^{2+} concentration on the corrosion of AISI 1018 steel in a 1 wt.% NaCl CO_2-saturated solution at 80°C and pH 6.6 under atmospheric pressure. They determined that the corrosion rate decreased with time at low Ca^{2+} content (up to 100 ppm) due to the formation of a mixed corrosion product layer ($FeCO_3$ and $Fe_xCa_{1-x}CO_3$). However, high concentrations of Ca^{2+} (10,000 ppm) were shown to increase the corrosion rate due to a non-protective corrosion product forming on the surface. Using XRD patterns, they were able to show that the isostructuality of $CaCO_3$ and $FeCO_3$ allowed the co-precipitation of Ca^{2+} and Fe^{2+} with CO_3^{2-}, altering the chemical and morphological properties. They were able to calculate the mole fraction of Ca^{2+} in $Fe_xCa_{1-x}CO_3$ and found that when the Ca^{2+} mole fraction approached 1, the protectiveness of the layer diminished in static conditions. Additionally, in static conditions with high Ca^{2+} content (10,000 ppm), localised corrosion was observed. Given that the Cl^- content in each experiment remained constant, it was suggested that Ca^{2+} was responsible for the initiation of localised corrosion, although this could also be attributed to acidification of the test solution due to initially rapid precipitation of $CaCO_3$ at higher Ca^{2+} concentrations.

It is clear that the presence of Ca^{2+} ions can result in the formation of mixed carbonate scales [13, 14, 17, 22, 23] which appear to have an effect on both general and localised corrosion

behaviour, particularly at atmospheric pressure in stagnant conditions. The precipitation of Mg-containing corrosion scales appears not to have been fully confirmed, although its presence within corrosion products has been reported. Furthermore, the effects of each ion have not been fully explored at elevated pressures where CO_2 exists in a supercritical state. It is also not clear in many instances how the corrosion products evolve over time and the implications this has for general corrosion. Therefore, this study is focused towards identifying the individual role of Cl^-, Ca^{2+} and Mg^{2+} ions on the formation, morphology and chemistry of corrosion products developed at high pressure (100 bar). In addition, the work seeks to determine the relationship between the corrosion products, solution chemistry and the extent of general and localised corrosion of carbon steel in supercritical CO_2-saturated brines. As previously mentioned, this work focuses on understanding the corrosion implications for carbon steel injection pipelines during the process of intermittent injection whereby brine rises back up the pipeline when injection ceases for a number of days. Such a situation results in a static fluid with a particular total volume being in contact with a specific internal area of pipeline. Such conditions are modelled within this work through specific closed vessel experiments with a high surface area to volume ratio, comparable with those encountered in a 17 to 18 inch carbon steel pipeline.

3. Materials and methods

3.1 Specimen material, preparation and test methodology

Test specimens were machined from carbon steel (API 5L X65) bars into discs of diameter 25 mm and thickness of 6 mm. The chemical composition of X65 steel and its microstructure are provided in Table 1 and Figure 1, respectively. Surface preparation consisted of wet-grinding the entire sample surface up to 800 grit silicon carbide abrasive paper, rinsing with distilled water, followed by acetone, high purity ethanol and drying with compressed air. Samples were then stored in a vacuum desiccator until needed and weighed immediately before use on an electronic balance to an accuracy of 0.01 mg before suspending inside the autoclave. Two samples were placed within the autoclave for each individual test, generating a total surface area of approximately 28 cm^2 exposed to 300 ml of solution.

Table 1: Elemental composition of X65 carbon steel (wt.%)

C	Si	Mn	P	S	Cr	Mo	Ni

0.12	0.18	1.27	0.008	0.002	0.11	0.17	0.07
Cu	**Sn**	**Al**	**B**	**Nb**	**Ti**	**V**	**Fe**
0.12	0.008	0.022	0.0005	0.054	0.001	0.057	Balance

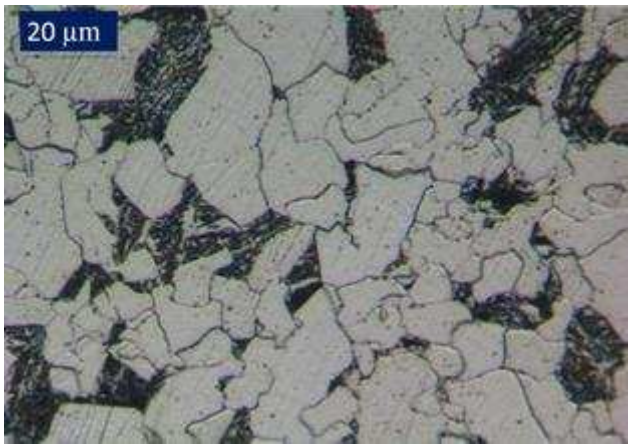

Figure 1: Optical microscope image of ferritic-pearlitic microstructure of API 5L X65 steel

The prepared solution used in each experiment was de-aerated with CO_2 in a separate container for a minimum of 12 hours prior to testing. Two specimens were suspended within the autoclave on a non-conducting wire whilst also ensuring they were not in contact with the walls of the cylinder to prevent galvanic effects. The prepared, CO_2-saturated solution was carefully delivered into the autoclave at ambient pressure and temperature and sealed. All lines to the autoclave were purged with CO_2 and evacuated to ensure removal of O_2 within the system. The CO_2 was then transferred into the autoclave and heated and pressurised to the correct temperature and pressure. The starting point of the test was taken from the point at which the autoclave reached the required temperature and pressure. The different solution compositions evaluated within this study are provided in Table 2. The required Ca^{2+} and Mg^{2+} concentration was achieved through the addition of calcium chloride di-hydrate ($CaCl_2 2H_2O$) and magnesium chloride hexa-hydrate ($MgCl_2 6H_2O$), respectively. The Cl^- content in each test was maintained at 35,249 ppm through the addition of NaCl. Only one experiment was performed at a lower Cl^- content to explore the effect of purely Cl^- on both layer formation, general corrosion rate and pitting. All experiments were performed under static conditions for periods of either 6, 24, 48 or 96 hours.

Table 2: Chemical composition of solutions and experimental parameters considered in this study

Cl^- (ppm)	Ca^{2+} (ppm)	Mg^{2+} (ppm)	T (°C)	Pco_2 (bar)	Immersion time (h)
4200	0	0	60	100	6, 24, 48 and 96
35,249	0	0			
	1,000	0			
	10,000	0			
	0	1,000			
	0	10,000			

Upon completion of each test, the specimens were dried thoroughly using an air gun. They were then weighed before being chemically cleaned to remove all traces of corrosion products before weighing again to determine the mass of corrosion product. The cleaning process consisted of wiping the surface with a cotton pad soaked in Clarke's solution (20 g antimony trioxide + 50 g stannous chloride + 1,000 ml 38% hydrochloric acid) in accordance with ASTM Standard G1-03.[24] This was followed by rinsing the sample with distilled water, followed by ethanol and drying with compressed air.

The mass loss due to corrosion was determined from the mass difference before exposure and after cleaning.

The corrosion rates were calculated by using Equation (1):

$$V_c = \frac{87600\Delta m}{\rho A T} \quad (1)$$

where V_C is the corrosion rate of the sample in mm/year, Δm is the mass loss in grams, ρ is the density of the sample in g/cm^3, A is the exposed area in cm^2, T is the immersion time in hours and 87600 is a conversion factor to express the corrosion rate in units of mm/year.

It is extremely challenging to monitor the actual pH throughout the whole corrosion test due to the high pressure within the autoclave. However, the initial solution pH and ionic strength in the presence of various concentrations of Cl^-, Ca^{2+} and Mg^{2+} ions was predicted using MultiScale software and is provided in Table 3.[25] All the pH values were predicted at approximately 3.1, with ionic strength varying with the nature of each cation and its concentration.

Table 3: Predicted initial bulk pH of the different brines used in this study at 60°C and 100 bar

Cl^- (ppm)	Ca^{2+} (ppm)	Mg^{2+} (ppm)	Predicted Ionic Strength using MultiScale (M)	Predicted pH using MultiScale
4200	0	0	0.19	3.11
35,249	0	0	1.01	3.06
	1,000	0	1.04	3.06
	10,000	0	1.27	3.06
	0	1,000	1.06	3.07
	0	10,000	1.43	3.12

3.2 *Scanning electron microscopy (SEM)*

SEM was conducted on samples using a Carl Zeiss EVO MA15 SEM to assess coverage and topography of corrosion products. All images were collected at an accelerating voltage of 20 kV and at a working distance of approximately 8 mm.

3.3 *X-ray diffraction (XRD)*

The XRD patterns for each sample were collected using a PANalytical X'pert multipurpose diffractometer, employing Cu Kα radiation (from a generator operating at 40 mA and 40 keV) with an active area of 10 x 10 mm programmable di-vergence slits. Scans were performed over a range 2θ = 10 to 70° using a step size of 0.033 per second, with a total scan time of approximately 50 minutes.

4. Results and discussion

4.1 Effect of Cl^- content and exposure time on the general corrosion rate and film formation of X65 steel

Figure 2(a) shows the corrosion rates (determined from mass loss) for X65 carbon steel exposed to the supercritical CO_2-saturated NaCl solutions containing 4,200 ppm and 35,249 ppm Cl^- at various immersion times between 6 and 96 hours in a 100 bar system at 60°C. Figure 2(a) indicates that X65 has corrosion rates of 16.6 and 20.1 mm/year over the first 6 hours for Cl^- contents of 4,200 and 35,249 ppm, respectively. The corrosion rates then decrease with increasing immersion time. The final average corrosion rates observed over 96 hours are 3.1 and 3.8 mm/year for systems containing 4,200 ppm and 35,249 ppm Cl^-, respectively.

Similar corrosion rates were also observed by Zhang et al.[11] who tested X65 steel at 95 bar and 80°C within a supercritical CO_2-saturated brine. The corrosion rate in their work was recorded at 20.6 mm/year and reduced to 7.35 mm/year between 7 and 96 hours. The results here also correlate with the observations of Liu et al.[26] who studied the effect of Cl^- concentration from 0 to 60,000 ppm on carbon steel in that the corrosion rate increased with Cl^- content. The results also illustrate that maintaining the Cl^- content is important to ensure the correct conclusions are drawn about the role of Ca^{2+} and Mg^{2+} on general corrosion rate.

One important aspect to consider in these experiments is the evolution of solution chemistry and the change in solution pH over time. Figure 2(b) shows the predicted changes in concentration of Fe^{2+} in the bulk solution. These were determined based on the difference in Fe^{2+} ions introduced to the bulk solution from the corrosion process (determined from the overall mass loss) and that consumed from the bulk solution as a result of precipitation onto the steel surface (determined from the corrosion product mass). The approximated Fe^{2+} concentration in the bulk solution was then entered into MultiScale to predict the evolution in solution pH with time, which is also provided in Figure 2(b). Note that this form of analysis assumes no bulk precipitation within the solution, which was a valid assumption based on visual inspection of the solution immediately after all tests were completed.

Referring to Figure 2(b),

For the high pressure conditions considered, the calculated increase in pH is less than 0.2 in all cases. Beyond 24 hours, the pH in each environment was stable and differed by ~0.1 between both experiments. Obviously, these values are only predictions and the complexities associated with measuring pH under such high pressure conditions meant that these calculated values could not be experimentally validated.

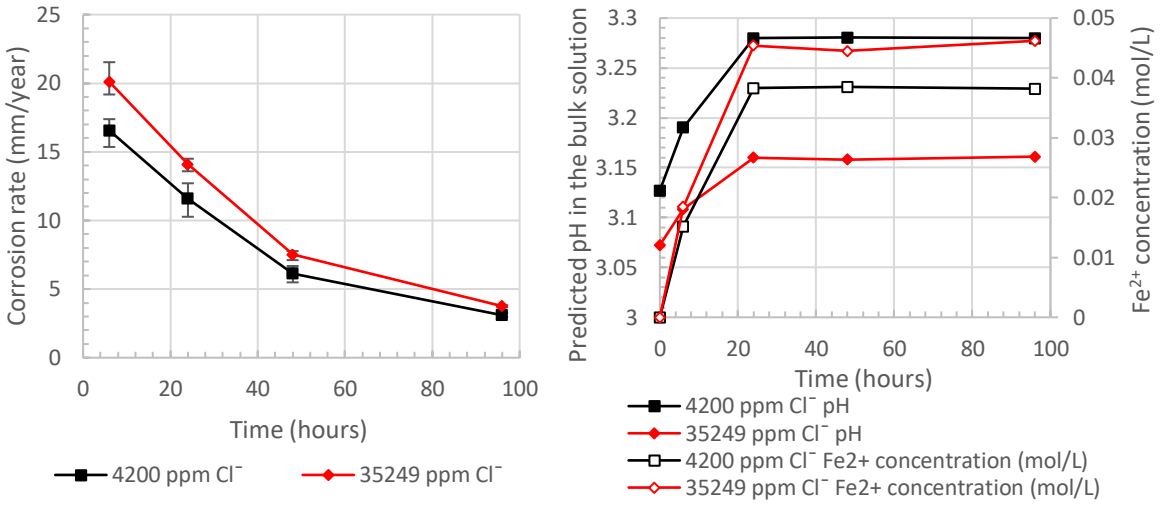

(a) **(b)**

Figure 2: (a) General corrosion rates and (b) pH/Fe^{2+} concentration in the bulk solution as a function of time for X65 carbon steel exposed to supercritical CO_2-saturated brine containing either 4,200 ppm or 35,249 ppm Cl^- at 60°C and 100 bar for periods between 6 and 96 hours.

Figure 3 shows the SEM images (top view and cross-sections) of X65 samples exposed to the two different concentrations of the NaCl-containing, supercritical CO_2-saturated brine. For both conditions, an iron carbide (Fe_3C) layer initially reveals itself on the steel surface over the first 6 hours (Figures 3(a) and 3(c)) as a result of the preferential dissolution of the ferrite phase within the steel microstructure. After 96 hours, the steel surfaces were entirely covered with a crystalline product, as shown in Figures 3(b) and 3(d). This product is shown to be exclusively $FeCO_3$ later in this work using X-ray diffraction (XRD) patterns. Despite the difference in initial corrosion rate between the two environments, the surface morphology, thicknesses of the layer (55-65 µm) and final corrosion rate are very similar at the end of the experiment. However, the $FeCO_3$ layer is marginally thicker and less uniform in thickness across the steel surface at the higher Cl^- content. These observations are in alignment with Liu et al.,[26] who studied the effect of Cl^- concentration from 0 to 92,520 ppm on the corrosion behaviour of carbon steel at 20 bar and 100°C. Their results showed that the thickness of the corrosion product layer increased and became less compact as Cl^- ion concentration increased from 0 to 15,420 ppm. It is likely in this scenario that the increased precipitation is attributed to the increased corrosion rate and flux of Fe^{2+} into the solution and not the ionic strength, as increased ionic strength has been reported to reduce the propensity for $FeCO_3$ to precipitate from the solution[4].

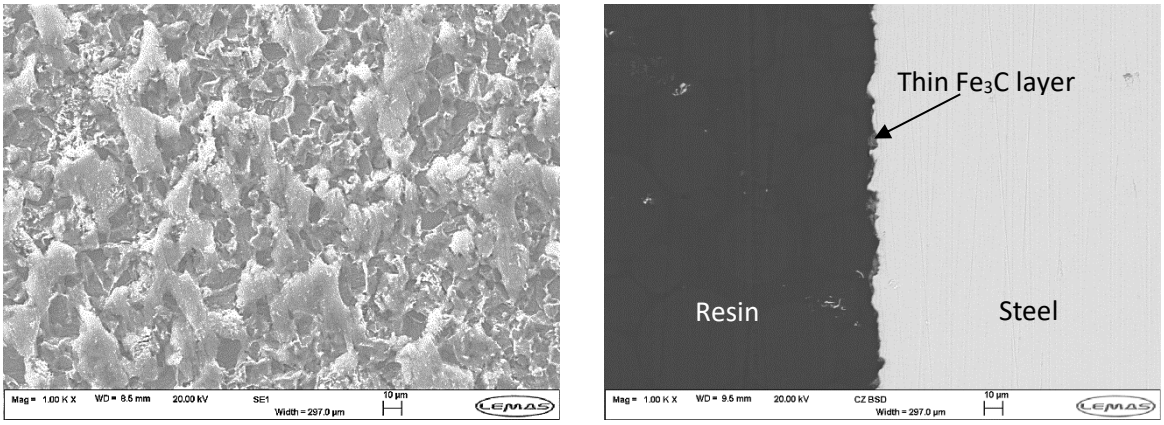
Thin Fe_3C layer
Resin
Steel

(a)

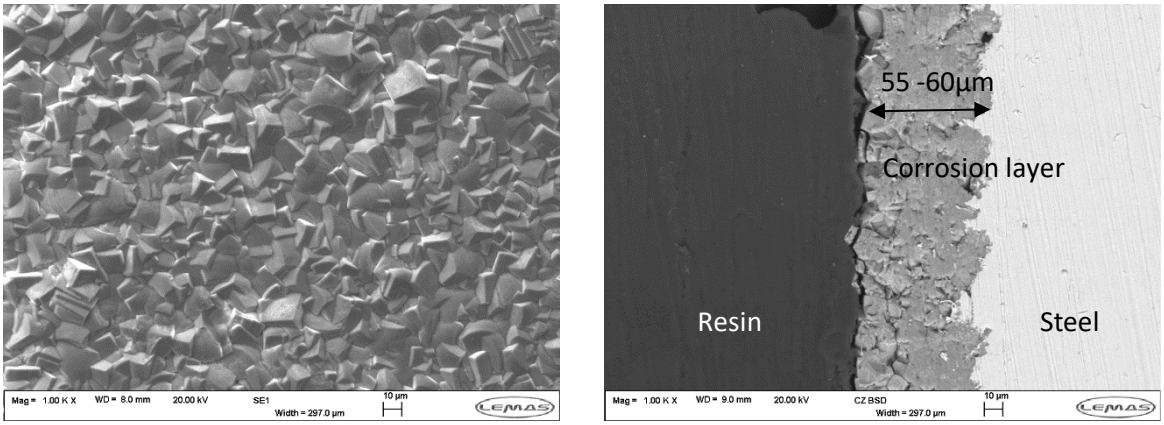
55 -60µm
Corrosion layer
Resin
Steel

(b)

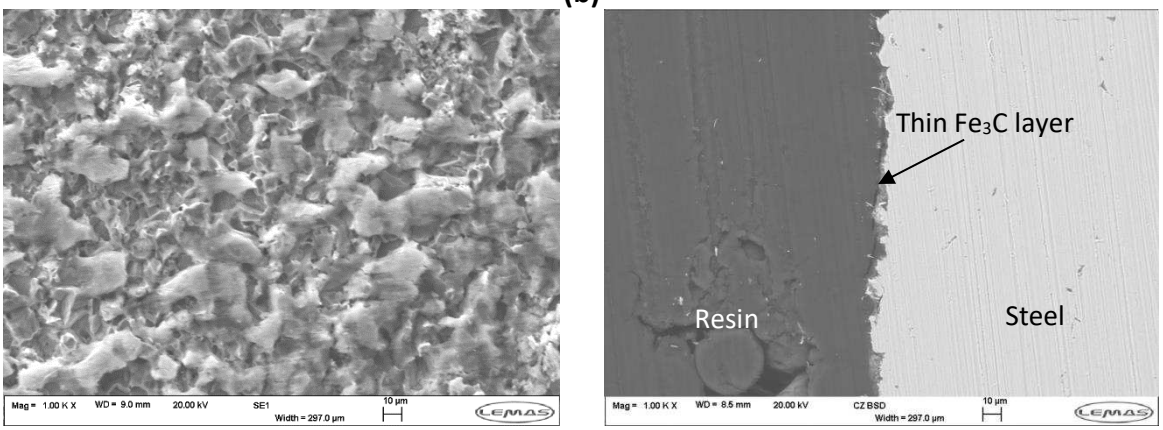
Thin Fe_3C layer
Resin
Steel

(c)

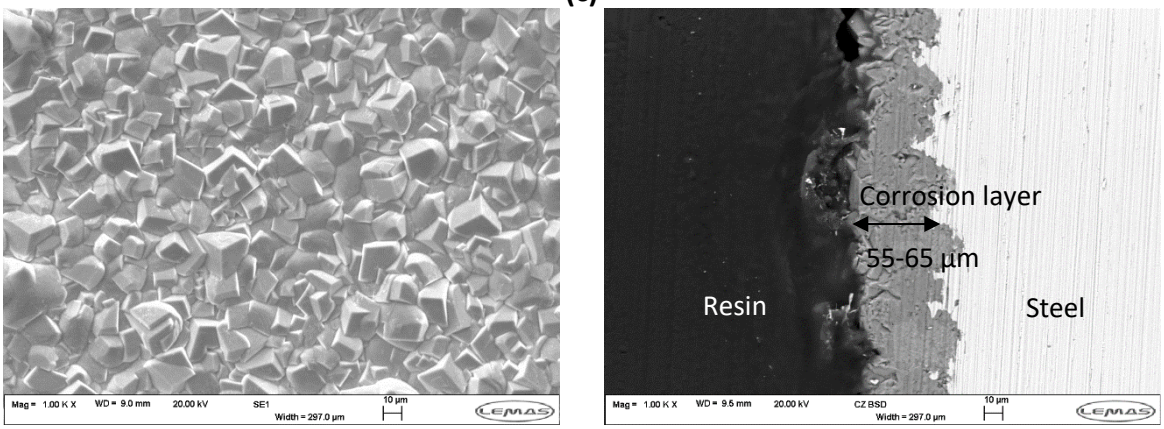
Corrosion layer
55-65 µm
Resin
Steel

(d)

Figure 3: SEM images (top view and cross-section) of X65 samples exposed to supercritical CO_2-saturated brines containing 4,200 ppm Cl^- for (a) 6 hours and (b) 96 hours, and 35,249 ppm Cl^- for (c) 6 hours and (d) 96 hours at 60°C and 100 bar.

4.2 Effect of varying Ca^{2+} and Mg^{2+} content on general corrosion rate and film formation of X65 steel

The influence of exposure time (6 to 96 hours) and addition of both 1,000 and 10,000 ppm of Ca^{2+} and Mg^{2+} individually on the general corrosion behaviour of X65 carbon steel for a constant Cl^- content of 35,249 ppm is shown in Figure 4. In the absence of a protective layer (the first 6 hours of testing), the addition of both divalent cations has a clear effect on the general corrosion rate. The addition of Ca^{2+} serves to reduce the general corrosion rate from 20.1 mm/year to 17.6 and 16.5 mm/year for addition of 1,000 and 10,000 ppm Ca^{2+}, respectively. However, the addition of Mg^{2+} accentuates general corrosion, increasing it from 20.1 mm/year to 21.0 and 22.0 mm/year for the addition of 1,000 and 10,000 ppm Mg^{2+}. As all the experiments progress and the precipitation of corrosion products begin to stifle the dissolution of iron from the steel surface, the corrosion rates for each experimental condition begin to converge toward an average value below 4 mm/year over 96 hours, with the exception of the test at 10,000 ppm Mg^{2+} which remains above 5 mm/year. In relation to the evolution of pH in these experiments, it is more challenging to accurately predict in these environments as a result of the complicated brine chemistry and precipitation of more complex corrosion products. However, predicted pH for the NaCl solution over time indicated a change of 0.2 from 0 to 96 hours. Given that the levels of corrosion are similar and that no precipitation was observed in the bulk solution for any of these experiments in Figure 4, it is anticipated that the changes in pH of the more complex brines are similar to that of the high concentration NaCl solution shown in Figure 2(b), although this cannot be confirmed without measurement.

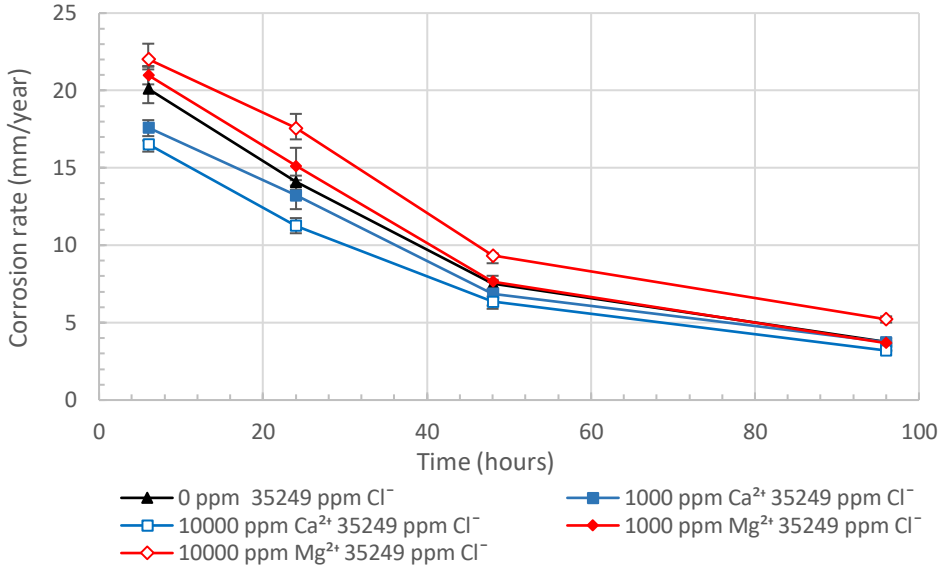

Figure 4: General corrosion rate as a function of time for X65 carbon steel exposed to supercritical CO_2-saturated brines containing different levels of Ca^{2+} and Mg^{2+} for a constant Cl^- content of 35,249 ppm at 60°C and 100 bar for periods between 6 and 96 hours.

4.3 Effect of Ca^{2+} addition on corrosion product layer morphology and composition

SEM images provided in Figure 5 show the influence of Ca^{2+} addition to the brine solution on the morphology of the corrosion product produced. The XRD patterns provided in Figure 6 indicate that $FeCO_3$ is the sole crystalline corrosion product in the absence of Ca^{2+} ions. However, addition of Ca^{2+} results in the $FeCO_3$ peaks shifting to lower values of 2θ with increasing Ca^{2+} addition. An additional experiment at 5,000 ppm Ca^{2+} has also been provided here to highlight the gradual shift with increasing concentration. The most intense Bragg reflection for $CaCO_3$ and $FeCO_3$ relates to the (104) Miller plane. These are located at 2θ values of 29.42° and 32.07° for $CaCO_3$ and $FeCO_3$, respectively. The gradual shift of the (104) peak, as well as the other visible peaks from their $FeCO_3$ positions towards their corresponding $CaCO_3$ equivalents is consistent with the substitution of Ca^{2+} for Fe^{2+} into the lattice. The isostructurality of both $CaCO_3$ and $FeCO_3$ is able to facilitate this co-precipitation and modify the morphological and chemical properties. The presence of Ca within the scale also results in the absence of a number of lower intensity peaks within the XRD pattern, with only two planes being detected overall within the XRD patterns for the addition of 10,000 ppm Ca^{2+} to the brine solution. Furthermore, the remaining peaks which have not diminished have become sufficiently broader. Both these observations can be attributed to the presence of Ca

and its heterogeneous distribution within the corrosion product layer. This interaction with the $FeCO_3$ lattice also promotes a change in crystal morphology from cubic crystals (Figure 5(b)) to globular structures comprising of much finer crystals (Figure 5(f)).

In terms of the protective capabilities of the layers developed, Figures 5(a), (c) and (e) show the effect of different levels of Ca^{2+} addition on the layer structure and morphology after an exposure time of 24 hours. There is clearly an increase in the porosity and spacing between individual crystals with increase in Ca^{2+} on the top surface of the corrosion product layer at this time period. However, the percentage reduction in general corrosion rate between 6 and 24 hours is very similar (25-30%), indicating that the layers afford very similar levels of protection. This also indicates that the porosity of the outer crystals in the corrosion product give a false indication as to the protectiveness of the layer and that it is the nature of the layer closer to the surface which must play the predominant role in influencing the corrosion behaviour.

Considering the percentage reduction in corrosion rate from 6 hours to 96 hours for the 0, 1,000 and 10,000 ppm Ca^{2+} experiments in Figure 3, the corrosion rate reduces by ~80% for all three tests, indicating very similar levels of layer protection across all conditions. Although the presence of Ca^{2+} changes the morphology and chemistry of the layer, the overall effect on general corrosion rate is not significant under these conditions after 96 hours.

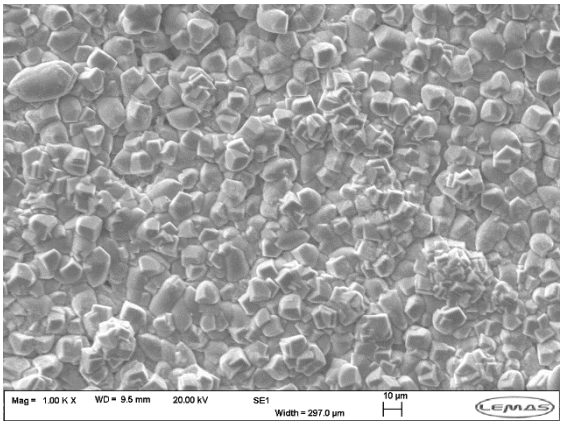

(a)

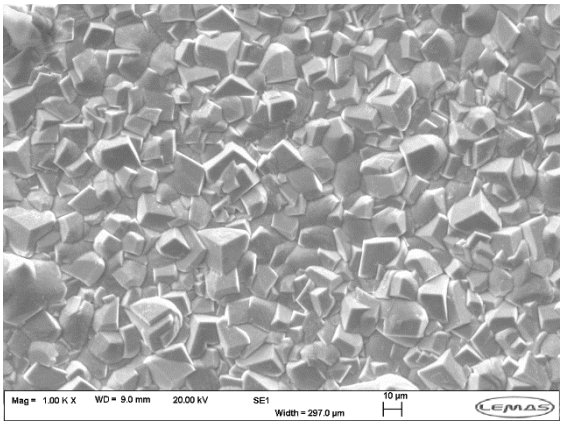

(b)

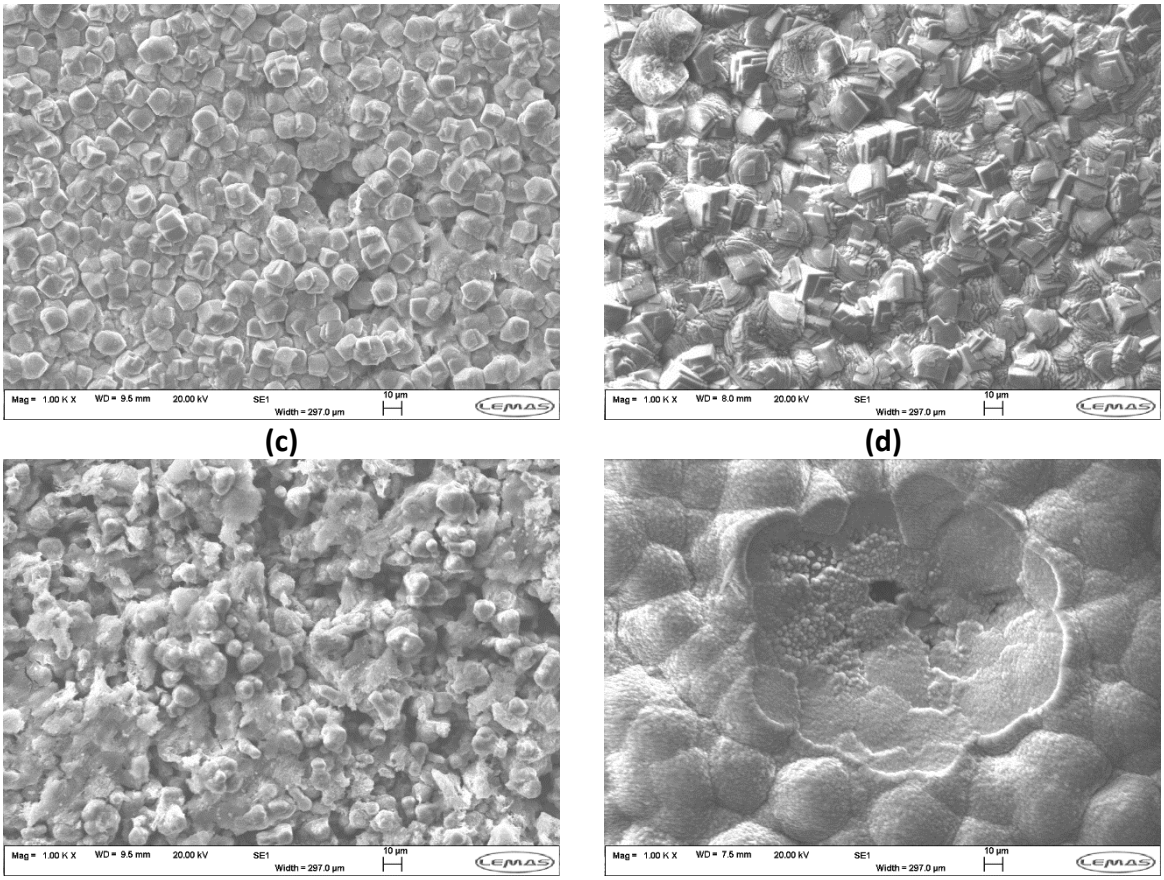

Figure 5: SEM images of X65 samples exposed to supercritical CO_2-saturated brines at 60 °C and 100 bar containing (a) 35,249 ppm Cl^- without Ca^{2+} for 24 hours, (b) 35,249 ppm Cl^- without Ca^{2+} for 96 hours, (c) 35,249 ppm Cl^- with 1,000 ppm Ca^{2+} for 24 hours, (d) 35,249 ppm Cl^- with 1,000 ppm Ca^{2+} for 96 hours, (e) 35,249 ppm Cl^- with 10,000 ppm Ca^{2+} for 24 hours, and (f) 35,249 ppm Cl^- with 10,000 ppm Ca^{2+} for 96 hours.

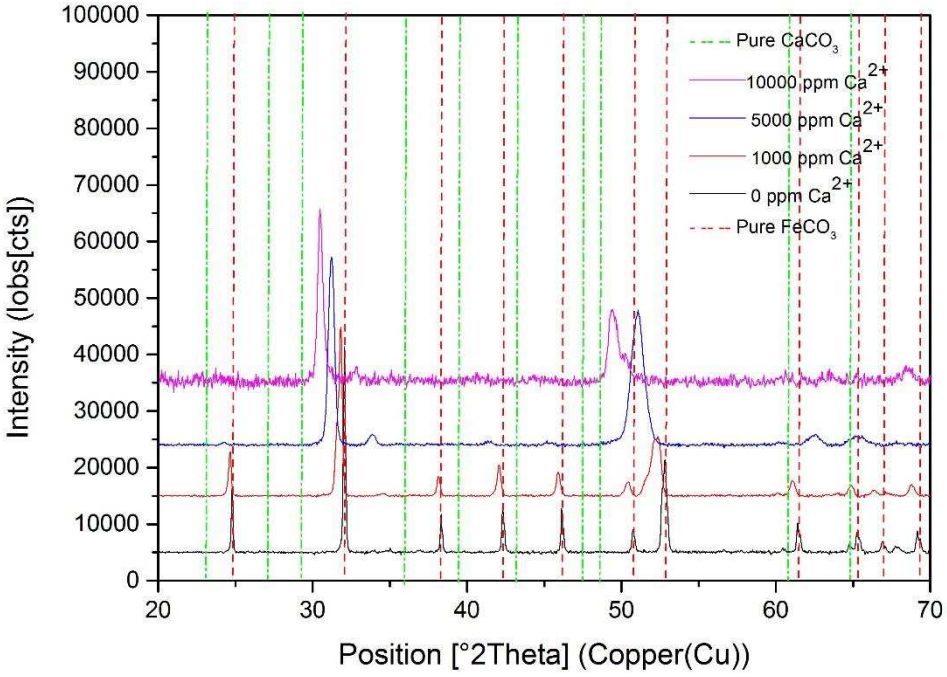

Figure 6: XRD patterns of X65 samples exposed to supercritical CO_2-saturated brines containing different levels of Ca^{2+} ions after 96 hours at 60°C and 100 bar; reference lines for the pure minerals are provided from the literature[4, 18]

4.4 Effect of Mg^{2+} addition on corrosion product layer morphology and composition

SEM images shown in Figures 7(a), (c) and (e) show that the addition of Mg^{2+} results in a more open structured outer layer after 24 hours of exposure. After 96 hours (Figures 7(b), (d) and (f)), the layer structure and porosity of the top section of the layer appear similar. Referring to Figure 4, the corrosion rates of the steel beneath these layers after 96 hours is similar, with the test at 10,000 ppm Mg^{2+} having a slightly higher corrosion rate at the end of the experiment.

Initial examination of the XRD patterns provided in Figure 8(a) suggest that the corrosion product formed on the X65 steel in all Mg^{2+}-containing brine experiments was purely $FeCO_3$. However, closer inspection of the (104) peak (Figure 8(b)) reveals that there is both a noticeable shift to higher values of 2θ, as well as broadening of the peaks, creating signs of asymmetry at the base with increasing Mg^{2+} content in the brine solution. The unit cell for $MgCO_3$ has dimensions particularly close to that of $FeCO_3$ due to the similarity in cation radii between Mg^{2+} and Fe^{2+}, with the former being slightly smaller than the latter. This means that

substitution of Mg^{2+} for Fe^{2+} in the $FeCO_3$ lattice results in the XRD peaks moving to slightly higher 2θ values. This observation is in contrast to the effect of Ca^{2+} substitution, where the larger Ca^{2+} radii compared to Fe^{2+} results in the peaks shifting to lower 2θ values. Furthermore, considering the location of the (104) peaks for $MgCO_3$ (32.67°), $FeCO_3$ (32.07°) and $CaCO_3$ (29.42°), it is clear that for the same level of Mg^{2+} or Ca^{2+} concentration within the layer, the substitution of Mg^{2+} would result in a much less dramatic shift in XRD peaks compared to Ca^{2+}. Nonetheless, Figure 8(b) indicates a noticeable shift and broadening in the (104) peak to higher 2θ values when the corrosion product develops in the solution containing 10,000 ppm Mg^{2+}. Broadening of the (104) peak for the 1,000 ppm Mg^{2+} experiment can also be observed, despite the highest intensity point on the peak matching that for $FeCO_3$. The suggested existence of Mg^{2+} within the $FeCO_3$ layer is supported by subsequent energy-dispersive x-ray (EDX) results shown later. Such little concentration of Mg at both conditions results in a less significant change in crystal morphology from introducing 10,000 ppm Mg^{2+} into the brine solution, as shown in Figures 7(b), (d) and (f), which reflect the surface condition after 96 hours.

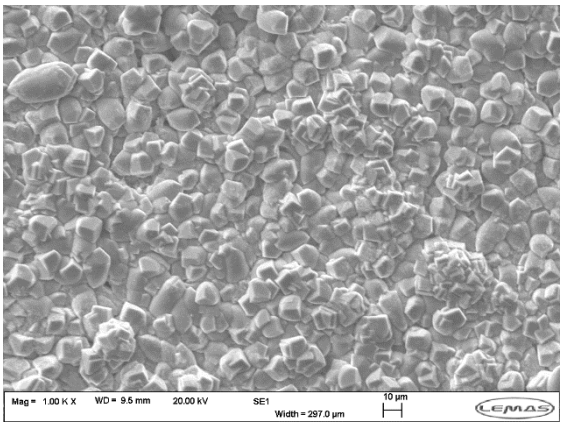

(a)

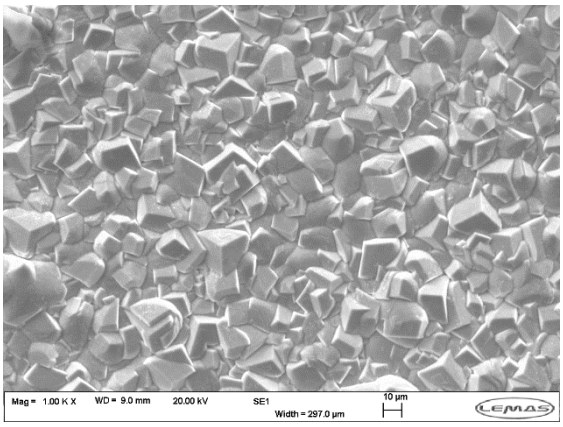

(b)

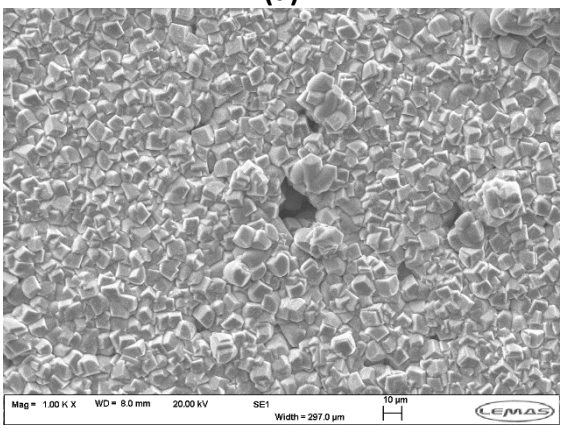

(c)

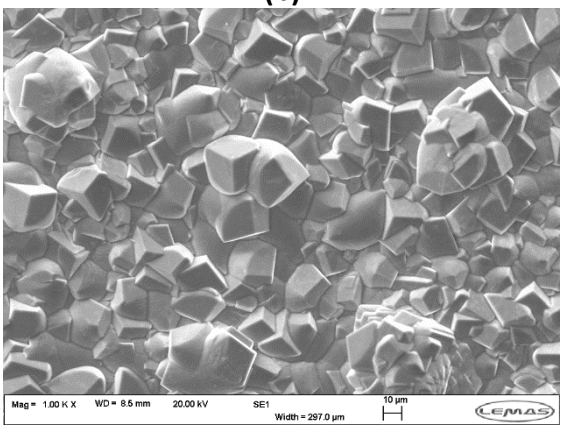

(d)

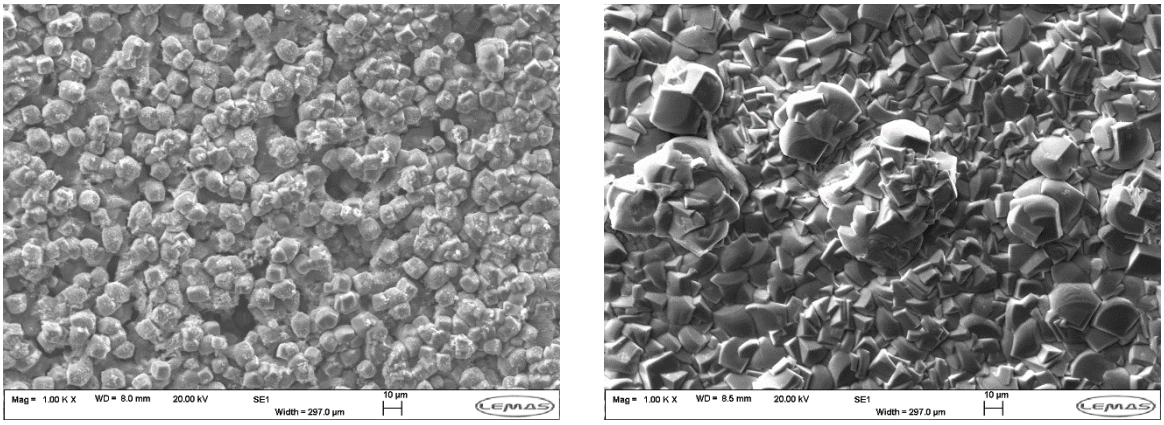

(e) **(f)**

Figure 7: SEM images of X65 samples exposed to supercritical CO_2-saturated brines at 60 °C and 100 bar containing (a) 35,249 ppm Cl^- without Mg^{2+} for 24 hours, (b) 35,249 ppm Cl^- without Mg^{2+} for 96 hours, (c) 35,249 ppm Cl^- with 1,000 ppm Mg^{2+} for 24 hours, (d) 35,249 ppm Cl^- with 1,000 ppm Mg^{2+} for 96 hours, (e) 35,249 ppm Cl^- with 10,000 ppm Mg^{2+} for 24 hours, and (f) 35,249 ppm Cl^- with 10,000 ppm Mg^{2+} for 96 hours.

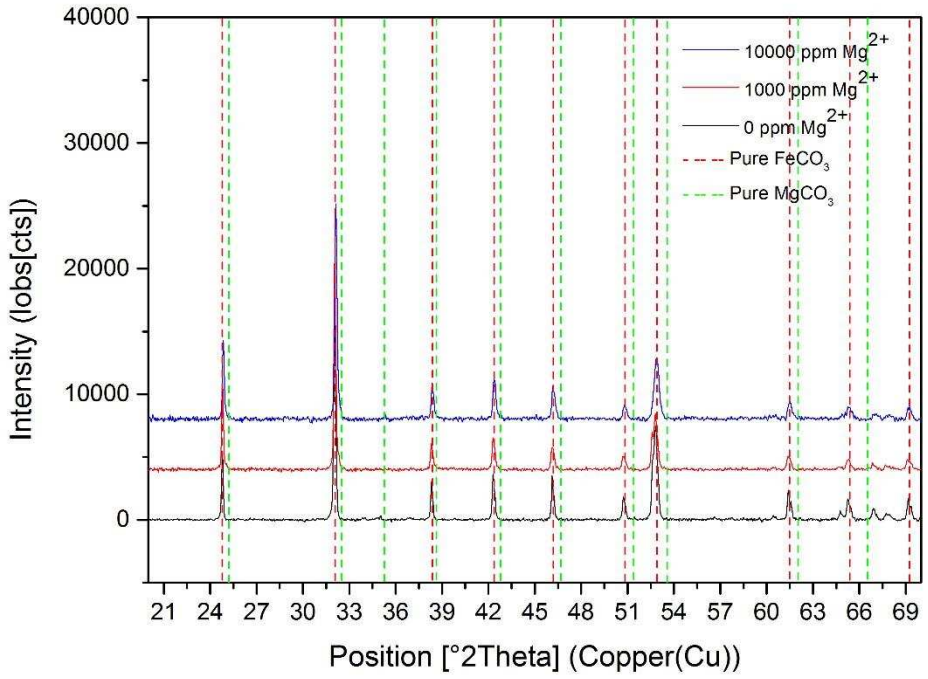

(a)

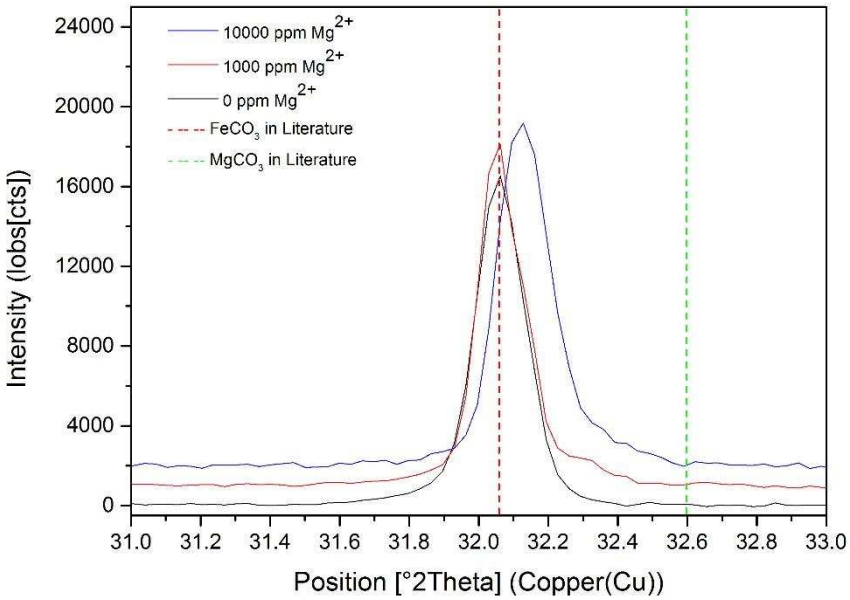

(b)

Figure 8: XRD patterns of X65 samples exposed to supercritical CO_2-saturated brines containing different levels of Mg^{2+} ions after 96 hours at 60°C and 100 bar; reference lines are provided from the literature. (a) 2θ ranging from 20 to 70° and (b) 2θ ranging from 31 to 33°; reference lines for the $FeCO_3$ and $MgCO_3$ are provided from the literature[4, 17]

4.5 Comparison of corrosion product thickness/composition and relation to brine chemistries

The initial results obtained from this study showed that Cl^-, Ca^{2+} and Mg^{2+} ions in the solution play an important role on the formation and morphology of corrosion product layers and the corrosivity of the solution. This section of the work explores the cross-sectional images of the corrosion products produced and their composition to establish links with the corrosion behaviour after 96 hours.

4.5.1 Cl^- effect

Figure 8 shows the SEM cross-section analysis of the layers formed on the samples exposed to the supercritical CO_2-satuated solution in the presence of various concentrations of Cl^-, Ca^{2+} and Mg^{2+} ions at 60°C and 100 bar for 96 hours. The thickness of the corrosion products in the presence of 4,200 and 35,249 ppm Cl^- are approximately 55-60 and 55-65 µm, respectively. The greater average thickness for the higher Cl^- content is logical given that the

corrosion rate in these experiments produces a greater flux of Fe^{2+} into the solution, enabling more precipitation back onto the steel surface (as discussed previously). Referring back to Figure 2, the additional thickness of the layers at higher salinity produced no significant increase in protection to the steel surface over 96 hours.

4.5.2 Ca^{2+} effect

The effect of 1,000 ppm and 10,000 ppm Ca^{2+} addition to the brine solution on the corrosion product structure is illustrated in the cross-section images provided in Figures 9(c) and (d). EDX area measurements below each micrograph indicate that Ca^{2+} was detected within the corrosion products, supporting the observations from XRD patterns where Ca^{2+} was shown to exist within the $FeCO_3$ lattice, producing $Fe_xCa_{1-x}CO_3$. Figure 10 shows cross-sections of the corrosion product layers produced in the absence (Figure 10(a)) and presence (Figure 10(b)) of 10,000 ppm Ca^{2+} which were made using a focused ion beam SEM. The EDX maps of the image in Figure 10(b) shows that the Ca concentration in the layer is not evenly distributed, corroborating with the broadening of the XRD peaks in Figure 6 with increasing Ca^{2+} concentration, highlighting the heterogeneity of the layer.

The intensity of the Ca peak in the EDX scans in Figures 9(c) and (d) also increases in conjunction with the Ca^{2+} content in the brine solution. This agrees with the extent of the shift of the XRD peaks within Figure 6, whereby a greater shift indicates a greater level of Ca substitution into the crystal lattice.

As in the work of Esmaeely et al.[14], the average concentrations of Ca within $Fe_xCa_{1-x}CO_3$ can be determined from the XRD peak positions in Figure 6 (as well as from the area EDX scans) using Equations (2) to (7):

Firstly, the d-spacing value for the (104) peak corresponding to the mixed $Fe_xCa_{1-x}CO_3$ was obtained from the XRD pattern according to Bragg's law as shown in Equation (2):

$$d = \frac{n\lambda}{2sin\theta} \quad (2)$$

Where n is a positive integer and λ is the wavelength of the incident X-rays wave.

In the next stage of the calculation, $FeCO_3$ and $CaCO_3$ are isostructural and share a hexagonal lattice structure for which the d-spacing can be expressed as:

$$\frac{1}{d^2} = \frac{4}{3}\left(\frac{h^2 + hk + k^2}{a^2}\right) + \frac{l^2}{c^2} \quad (3)$$

where h, k and l are the Miller Indices corresponding to particular peaks and lattice planes, obtained from XRD data. The a and c values are unit cell edges, obtained by solving:

$$a^2 = \frac{2V}{c\sqrt{3}} \quad (4)$$

where V is the unit cell volume.

Assuming linear behaviour for Ca^{2+} substitution into the structure in terms of unit cell parameters and unit cell volume, the mole fraction (referred to as 'y' here) of Ca^{2+} in the lattice is calculated from Equations (5) and (6).[27]

$$c = 1.6885y + 15.373 \quad (5)$$

$$V = 74.107y + 291.34 \quad (6)$$

The final equation is generated by substituting Equations (4), (5) and (6) into Equation (3):

$$\frac{1}{d^2} = \frac{4}{3}\left(\frac{2.92456y + 26.62681}{148.214y + 582.68}\right) + \frac{16}{(1.6885y + 15.373)^2} \quad (7)$$

Based on the interpretation of the peak shifts in the XRD patterns, the Ca contents in each of the layers are 0.09, 0.28 and 0.58 for experiments with 1,000, 5,000 and 10,000 ppm Ca^{2+}.

Reviewing Figures 9(b), (c) and (d), the thickness of the corrosion products range from 50-65 µm in the presence of 0, 1,000 and 10,000 ppm Ca^{2+} ions, indicating that the divalent cation has little effect on the layer thickness. The similarity in both thickness and final corrosion rate after 96 hours in all three experiments indicates that the layers produced offer very similar protection to the steel surface in relation to general corrosion.

4.5.3 Mg^{2+} effect

Figures 9(e) and (f) show the SEM cross-section analysis of samples after exposure to the 1,000 and 10,000 ppm Mg^{2+}-containing brine solutions for 96 hours. In these experiments, a clearer increase in layer thickness with Mg^{2+} brine content is observed, correlating with the higher corrosion rate of the steel sample throughout the entire duration of the experiment. The product layer thickness increased from 50-65 µm to 65-75 µm as Mg^{2+} content was increased from 0 ppm to 10,000 ppm. Based on the EDX area scans of the sample cross-

section, the presence of Mg was detected within the corrosion products, but only in trace amounts. An average of the ratio of Mg to Fe suggested corrosion product compositions of $Fe_{0.96}Mg_{0.04}CO_3$ and $Fe_{0.94}Mg_{0.06}CO_3$ for the 1,000 ppm and 10,000 ppm Mg^{2+} solutions, respectively. Such low concentration of Mg^{2+} compared to Ca^{2+} within the corrosion products could at least be partly attributed to the higher solubility of $MgCO_3$ compared to $CaCO_3$ under these particular operating conditions, as discussed in the following section.

4.5.4 Solubility characteristics of $FeCO_3$, $CaCO_3$ and $MgCO_3$

The solubility constants for $FeCO_3$, $CaCO_3$ (calcite) and $MgCO_3$ reported in the literature have been determined by Benezeth et al.[28], Dorange et al.[29] and Benezeth et al.[30], respectively:

$$logK_{sp,FeCO_3} = 175.568 - \frac{6738.483}{T} + 0.0139T - 67.898logT \quad (8)$$

$$logK_{sp,Calcite} = -7.8156 - \frac{1502}{T} - 0.03111T + 5.518logT \quad (9)$$

$$logK_{sp,Magnesite} = 7.267 - \frac{1476.604}{T} - 0.033918T \quad (10)$$

where T is the temperature in degrees Kelvin. Comparing Equations (8) to (10) at 60°C, the K_{sp} values for $FeCO_3$, $CaCO_3$ (calcite) and $MgCO_3$ are 4.92×10^{-12}, 1.71×10^{-9} and 3.45×10^{-9}, indicating that $FeCO_3$ is by far the least soluble, followed by calcite, then magnesite at 60°C. Although not accounting for ionic strength effects on the activity of the species involved in the precipitation process and the corresponding effect on the saturation level of each mineral at the steel surface (the ratio of the product of the activities of the precipitating species relative to the phase solubility), the relative trends of these solubility values help to explain partly why Mg^{2+} appears to have less propensity to co-precipitate. That being said, the molar fraction of Mg in the corrosion product is 0.06 for a solution containing 10,000 ppm Mg^{2+}, while solutions with one order of magnitude less Ca^{2+} in the bulk solution (1,000 ppm) produces a mole fraction of 0.09. Considering that the solubility of $CaCO_3$ is only half that of $MgCO_3$ and the theoretical pH values of the solutions are very similar, it is perhaps surprising based on this comparison to find a lower Mg^{2+} molar concentration compared to Ca^{2+} within the corrosion products. This suggests that either the ionic strength has a profound influence on the relative activities of Ca^{2+} and Mg^{2+}, making $MgCO_3$ saturation levels at the steel surface considerably lower compared to $CaCO_3$ under these conditions, or that the saturation ratio of $FeCO_3$ to $CaCO_3$ and $FeCO_3$ to $MgCO_3$ in these environments does not hold a universal

correlation across both sets of carbonates with regards to predicting the film stoichiometry, i.e., a saturation ratio of 10:1 for both $FeCO_3$ to $CaCO_3$ and $FeCO_3$ to $MgCO_3$ does not imply the same level of Ca^{2+} and Mg^{2+} molar concentration in both corrosion products. This is logical given that the precipitation kinetics of $CaCO_3$ and $MgCO_3$ differ from one another and are likely to play a role in influencing the molar concentration observed within the layer. In fact, this notion was considered in detail by Alsaiari et al.[31] who studied the *bulk* precipitation of $Fe_xCa_{1-x}CO_3$ and theoretically derived an equation relating the solid solution stoichiometry to solution chemistry and the precipitation kinetics of each pure phase. Alsaiari et al.[31] demonstrated that the molar fraction of Fe (χ_{Fe}) relative to Ca within $Fe_xCa_{1-x}CO_3$ can be expressed in the form of a function:

$$\chi_{Fe} = \frac{1}{1 + k\frac{(a_{Ca^{2+}} - a_{Ca^{2+},eq})a_{Ca^{2+}}}{(a_{Fe^{2+}} - a_{Fe^{2+},eq})a_{Fe^{2+}}}} \quad (11)$$

where $a_{Ca^{2+}}$ is the activity of Ca in the system, $a_{Ca^{2+},eq}$ is the activity of Ca at equilibrium, $a_{Fe^{2+}}$ is the activity of Fe in the system, $a_{Ca^{2+},eq}$ is the activity of Fe at equilibrium and *k* is the ratio of rate constants for the precipitation of the two pure phases of $CaCO_3$ and $FeCO_3$:

$$k = \frac{k_{CaCO_3}}{k_{FeCO_3}} \quad (12)$$

Therefore, the composition of the produced layer is theoretically related to both the individual precipitation kinetics of each phase, their individual solubility characteristics and the activities of the ionic species participating in the precipitation reaction. However, it is also possible that the precipitation of species is capable of impairing the other in such an environment. Alsaiari et al. [31] also stated that the difference in characteristic water loss rate constant of the free ions in the solution, the difference in interfacial free energy of the pure end-members and the different values of the energy barriers may also play a critical role in the film chemistry, particularly when there is a small difference in saturation ratio between the precipitating phases.

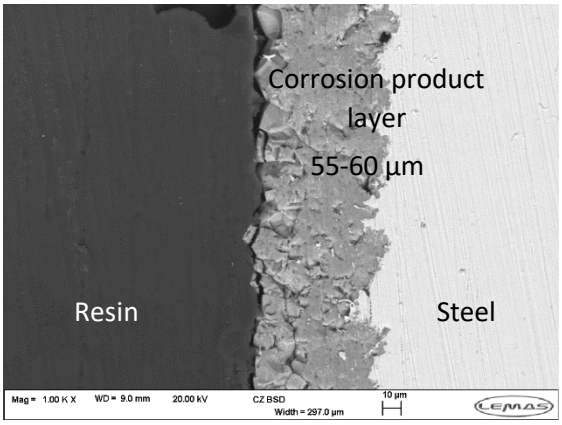
Corrosion product
layer
55-60 µm
Resin
Steel

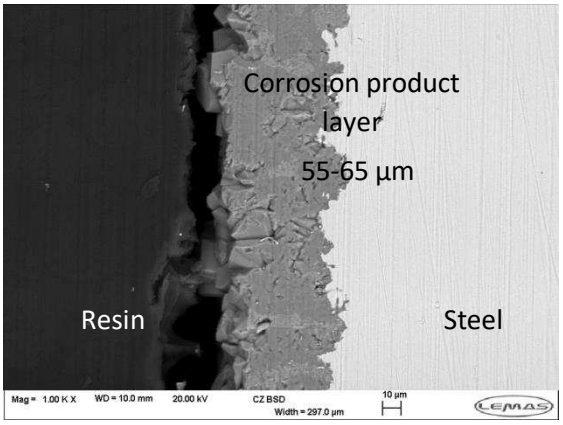
Corrosion product
layer
55-65 µm
Resin
Steel

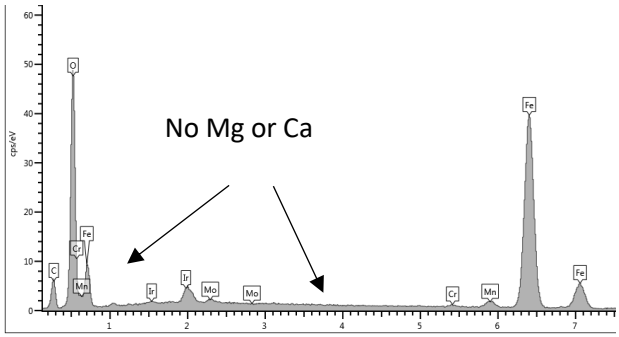
No Mg or Ca

(a)

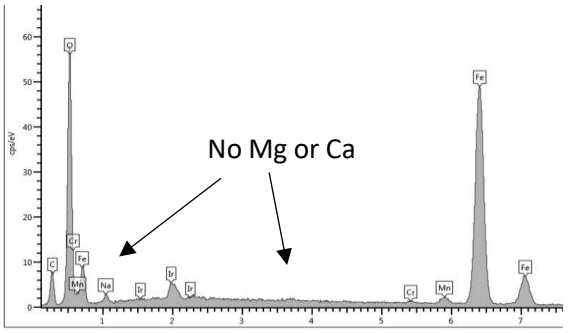
No Mg or Ca

(b)

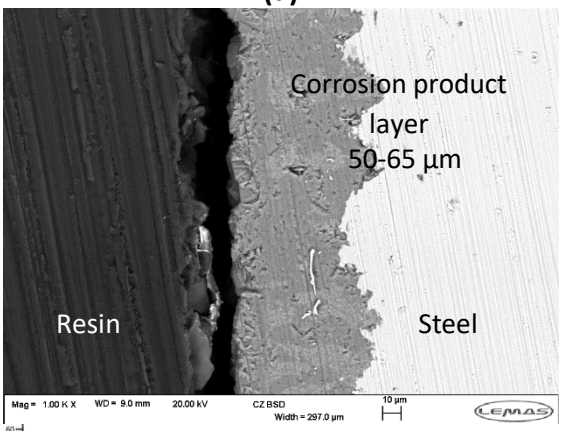
Corrosion product
layer
50-65 µm
Resin
Steel

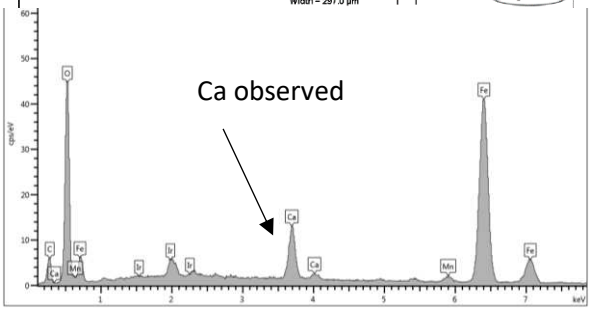
Ca observed

(c)

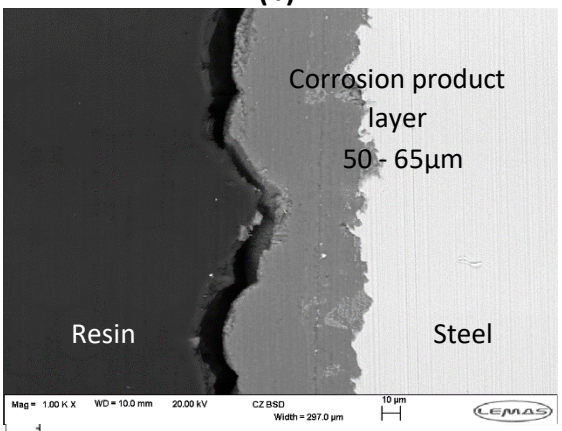
Corrosion product
layer
50 - 65µm
Resin
Steel

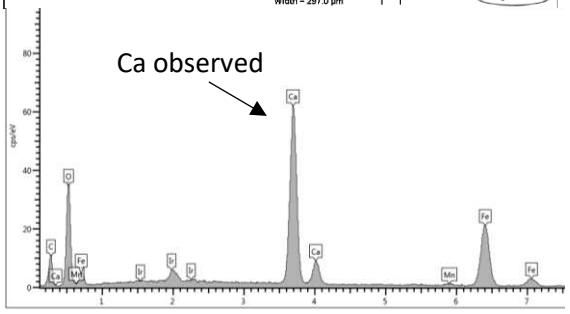
Ca observed

(d)

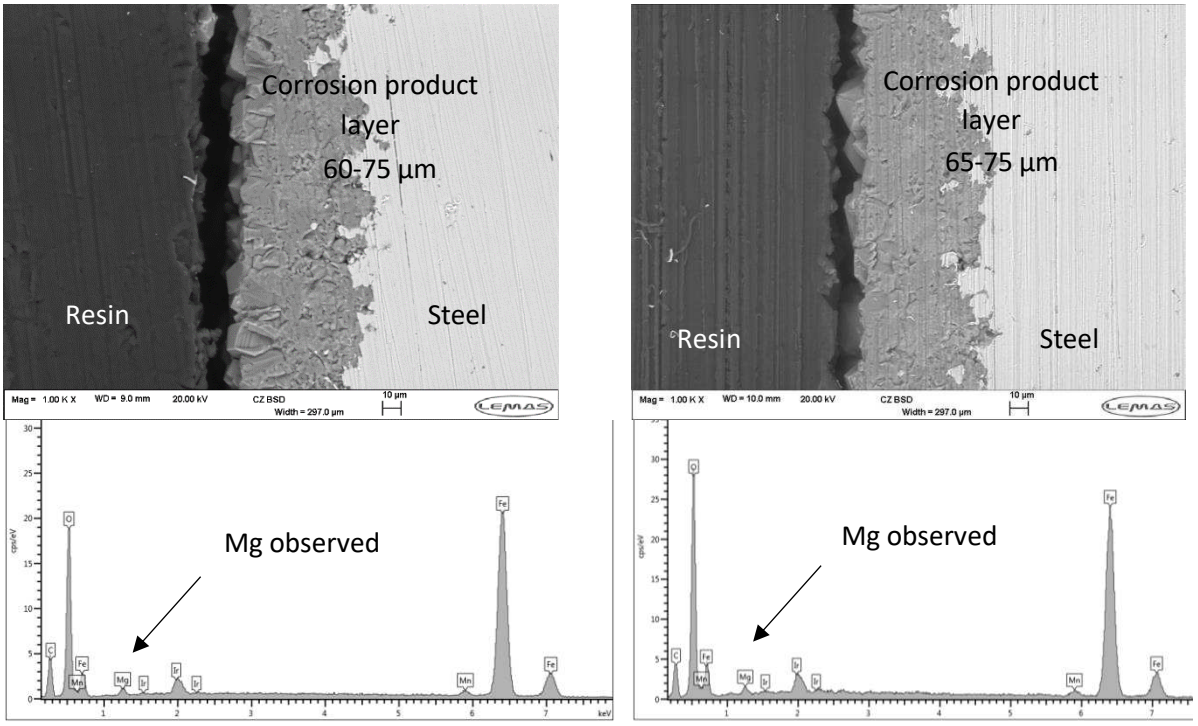

(e) **(f)**

Figure 9: SEM cross-section images and associated EDX area scans for X65 samples exposed to supercritical CO_2-saturated brines at 60°C and 100 bar for 96 hours containing (a) 4200 ppm Cl^-, (b) 35,249 ppm Cl^-, (c) 1,000 ppm Ca^{2+} and 35,249 ppm Cl^-, (d) 10,000 ppm Ca^{2+} and 35,249 ppm Cl^-, (e) 1,000 ppm Mg^{2+} and 35,249 ppm Cl^-, (f) 10,000 ppm Ca^{2+} and 35,249 ppm Cl^-.

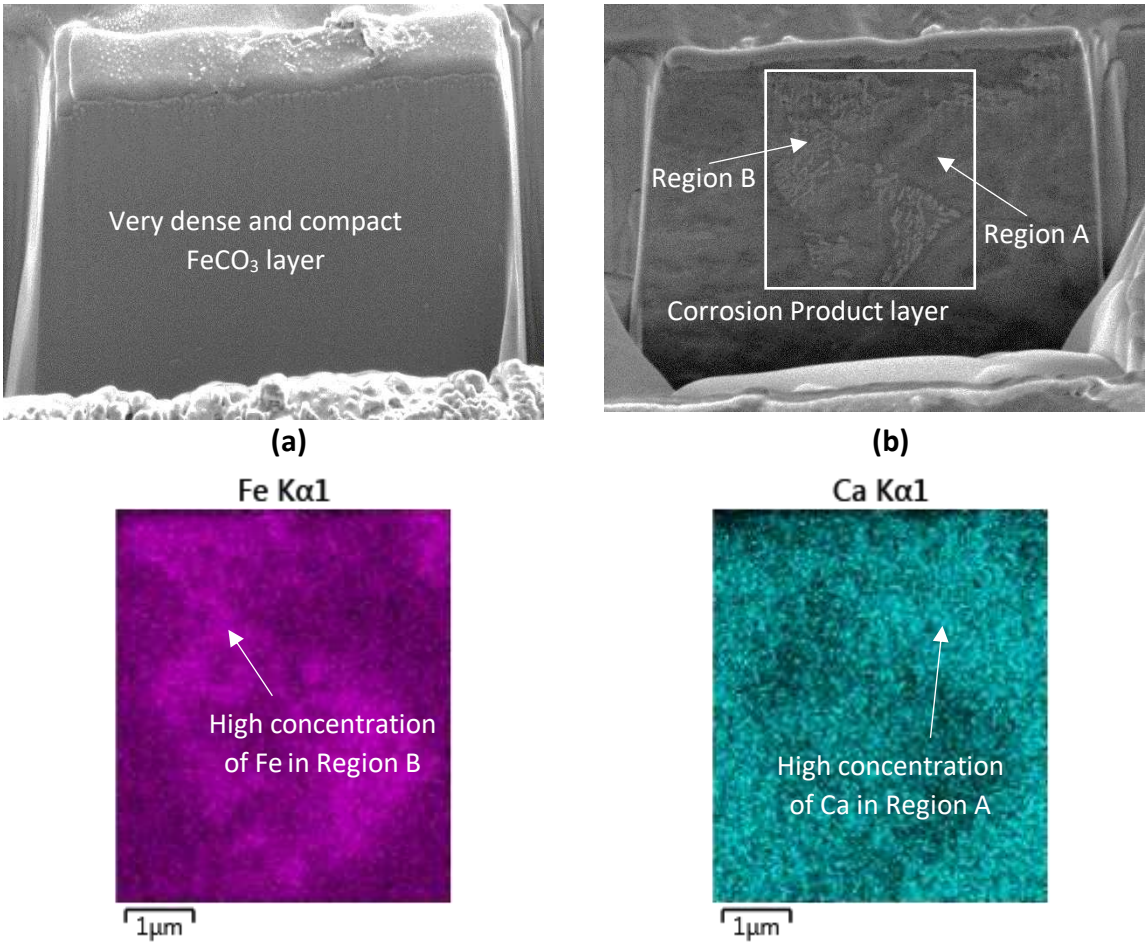

Figure 10: SEM images of samples exposed to supercritical CO_2-saturated solution at 60°C and 100 bar for 96 hours containing (a) 35,249 ppm Cl^-, (b) 10,000 ppm Ca^{2+} and 35,249 ppm Cl^- after sectioning the layer using a focused ion beam. (c) and (d) show the EDX maps of the area highlighted in Figure 10(b) for Fe and Ca, respectively.

4.6 Effect of brine chemistry on localised corrosion in comparison to general corrosion and their relation to film characteristics

Only a few authors have considered the extent of localised corrosion of carbon steels in environments containing Ca^{2+} and Mg^{2+} ions, with such work being performed at atmospheric pressure.[13, 19] This work focuses on contributing to the understanding of such ions on localised corrosion, as well as general corrosion through the application of non-contact profilometry.

In this study, steel samples were removed from every test condition after 6, 24, 48 and 96 hours, cleaned with Clarke's solution and profiled using white light interferometry. Multiple images from two samples exposed to each test condition were evaluated to enable

interpretation of the extent of pitting corrosion over 96 hours in each environment. Further details on the form of analysis undertaken is provided in a previous publication.[32]

Figure 11(a) shows both the general corrosion rate and localised penetration rate over 96 hours for all test conditions. The percentage efficiency of the corrosion product layers in terms of general corrosion rate reduction from 6 to 96 hours is provided at the base of each bar. The penetration rate was determined by converting the average pit/localised depth into mm/year based on the exposure time to the test solution, followed by adding this value onto the general thickness loss rate determined from mass loss measurement. The methodology assumes that the material loss due to pitting is considerably smaller than that associated with general corrosion, which has been shown to be a valid assumption for carbon steel pitting[33]. An example of the profilometry map produced from one scan is provided in Figure 11(b), and relates to the test environment containing 10,000 ppm Ca^{2+}.

Referring to the general corrosion rates and corrosion layer protectiveness in Figure 11(a), the level of protection afforded by each layer is approximately 80%, with little to distinguish between each layer in terms of their ability to reduce uniform corrosion. However, comparison of the total penetration rates reveals that increasing Cl^-, Ca^{2+} and Mg^{2+} all serve to increase the overall penetration rate. In the context of Mg^{2+}, a larger proportion of the total penetration is comprised of the general dissolution compared to the Ca^{2+}-containing tests and the pure NaCl brine experiments (which is reflected in pit depth measurements after 96 hours in Figure 12).

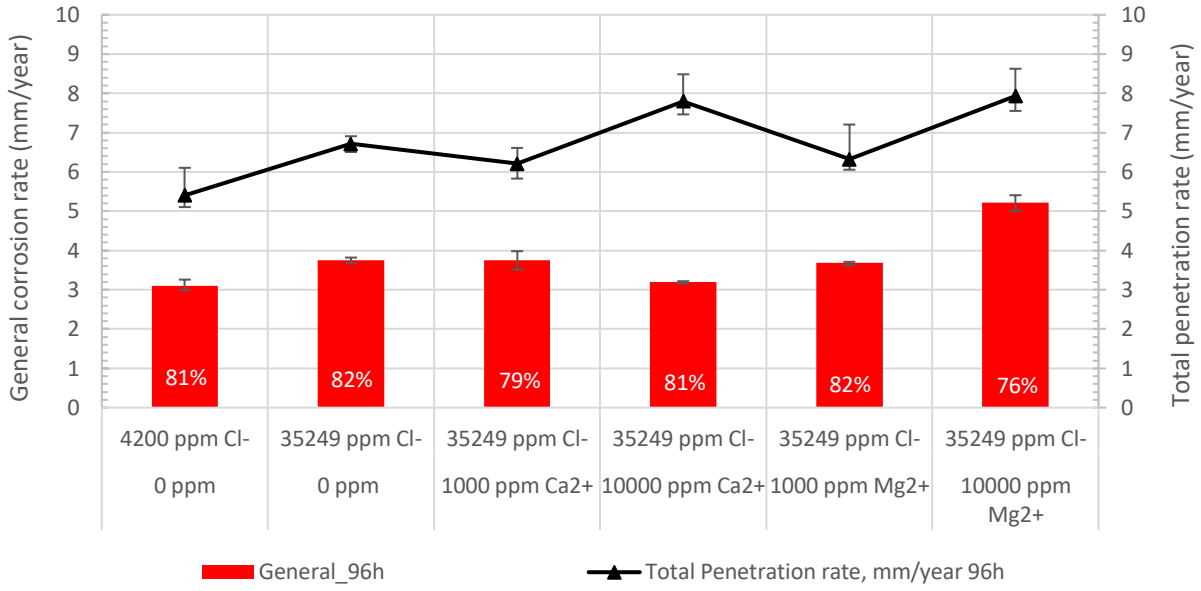

(a)

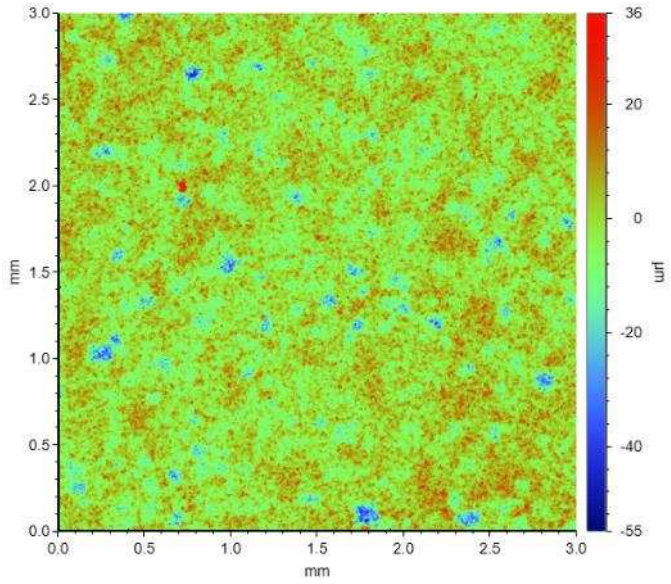

(b)

Figure 11: (a) General and localised corrosion rates of X65 carbon steel exposed to supercritical CO_2-saturated brine containing different levels of Cl^-, Ca^{2+} and Mg^{2+} at 60 °C and 100 bar for 96 hours; (b) example of profilometry map produced from interferometry measurements from the steel surface (environment containing 10,000 ppm Ca^{2+})

Although Figure 11(b) provides average localised corrosion rates over 96 hours, it does not provide information relating to the propagation of localised attack/pits. To complement Figure 11, Figure 12 shows the average localised/pit depth as a function of time from 6 to 96 hours for the experiments involving the high Cl^- and 10,000 ppm divalent cation

concentrations. The results show that pit propagation relative to the corroding steel surface is more favourable in the presence of Ca^{2+} ions, and that Cl^- content also encourages pit propagation. The presence of Mg^{2+} results in a higher general corrosion rate which masks the growth of pits relative to the corroded steel surface. For all conditions considered, the rate of growth of localised attack slows down as the corrosion product evolves. However, the rate of pit growth from 48 h to 96 hours is the highest in the presence of Ca^{2+}, suggesting that the layer or the mere presence of Ca^{2+} promotes localised attack. Further work is required to determine the underlying reason behind the difference in pit growth kinetics.

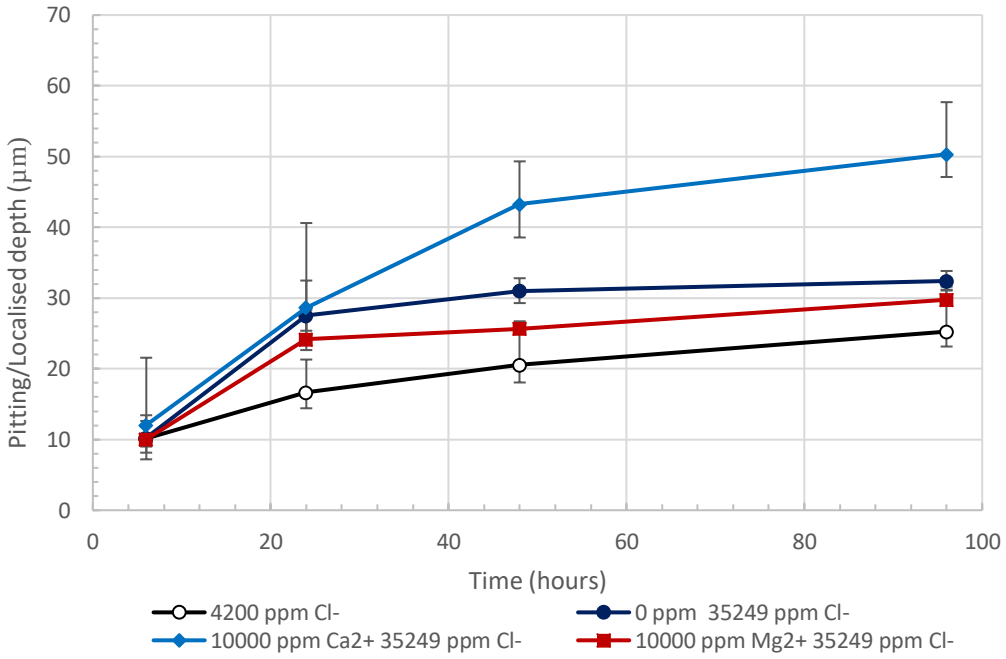

Figure 12: Pitting/localised depths for X65 steel samples exposed to supercritical CO_2-saturated brine containing different levels of Cl^-, Ca^{2+} and Mg^{2+} at 60 °C and 100 bar for immersion times between 6 and 96 hours.

5. Conclusions

The corrosion behaviour of X65 carbon steel was evaluated in supercritical CO_2-saturated water in the presence of different levels of Cl^- (4,200 and 35,249 ppm), Ca^{2+} (1,000 and 10,000 ppm) and Mg^{2+} (1,000 and 10,000 ppm) ions at 100 bar and 60°C, over immersion times between 6 and 96 hours. Particular focus was directed towards understanding the influence of the aforementioned cations on the on the formation and chemistry of corrosion products developed on the steel surface, as well as their effect on general and localised corrosion

618 behaviour when Cl^- content remained constant at 35,249 ppm. From this study, the following
619 can be concluded:

620 • Based on 6 hour experiments where protective corrosion products/scales were absent
621 from the steel surface, an increase in Cl^- content served to increase general corrosion.
622 Addition of Mg^{2+} also resulted in an increase in general corrosion, whereas the
623 addition of Ca^{2+} reduced general dissolution rates. Such effects produced by Mg^{2+} and
624 Ca^{2+} increased as the concentration of the divalent cations in the brine was raised from
625 1,000 to 10,000 ppm.
626 • General corrosion rates reduced with time in conjunction with the formation of
627 corrosion products in all test environments. The corrosion products formed on each
628 carbon steel surface exhibited different morphologies and compositions depending
629 upon the brine chemistry, but all layers provided approximately 80% reduction in
630 general corrosion rate.
631 • Iron carbonate ($FeCO_3$) was the only crystalline product to develop on the steel surface
632 in the presence of Cl^- (purely NaCl brine)
633 • The presence of Ca^{2+} within the brine resulted in the formation of iron-calcium
634 carbonate ($Fe_xCa_{1-x}CO_3$), confirmed using XRD measurements. The molar fraction of
635 Fe and Ca within the layer increased along with the Ca^{2+} content added to the brine.
636 • The presence of Mg^{2+} within the brine resulted in the formation of iron-magnesium
637 carbonate ($Fe_xMg_{1-x}CO_3$), which was also confirmed using XRD, but resulted in less
638 noticeable shifts in the produced XRD peaks within the collected patterns.
639 • Ca^{2+} demonstrated a much greater propensity to co-precipitate in conjunction with
640 $FeCO_3$ compared to Mg^{2+}. This was postulated to be attributed to a number of factors,
641 with the greater solubility of $MgCO_3$ compared to $CaCO_3$ being one of the likely reasons
642 under these test conditions.
643 • Other factors which were discussed that could potentially influence the stoichiometry
644 of the carbonate layers produced included the relative precipitation rates of the pure
645 minerals, the level of saturation of each phase (related to solubility and species
646 activity), as well as the difference in water loss rate constant of the free ions,
647 differences in interfacial energy of end-members and the energy barriers associated
648 with the combined precipitation process.

- Cl^-, Ca^{2+} and Mg^{2+} were shown to accentuate total penetration rate of carbon steel (i.e., pitting rate relative to the corroding steel surface plus the general thickness loss rate). However, the growth of pits relative to the corroding surface was shown to diminish, or even stabilise with time in all conditions.
- The more severe pit propagation under the test conditions evaluated in this study was observed in the presence of Ca^{2+}. Further study is required to determine the exact reasons behind accelerated pitting kinetics under these conditions.

6. References

1. M. Wilson, and M. Monea, *IEA GHG Weyburn CO_2 monitoring & storage project. Summary report 2000-2004.* 2004.
2. O. Yevtushenko, D. Bettge, S. Bohraus, R. Bäßler, A. Pfennig, and A. Kranzmann, *Corrosion behavior of steels for CO_2 injection.* Process Safety and Environmental Protection, 2014. **92**(1): p. 108-118.
3. A. Dugstad, *The importance of $FeCO_3$ supersaturation on the CO_2 corrosion of mild steels.* in CORROSION 92, 1992: NACE International. Paper no: 11072.
4. W. Sun and S. Nesic, *kinetics of Corrosion layer formation: Part 1-iron carbonate layers in CO_2 corrosion.* Corrosion: Vol. 64, No.4, pp.334-346. April 2008.
5. Farelas, F., B. Brown, and S. Nesic. *Iron Carbide and its Influence on the Formation of Protective Iron Carbonate in CO_2 Corrosion of Mild Steel*. in *CORROSION 2013*. 2013. NACE International. Paper no: 2291.
6. V. Ruzic, M. Veidt, and S. Nešić, *Protective iron carbonate films-Part 1: Mechanical removal in single-phase aqueous flow.* Corrosion, 2006. **62**(5): p. 419-432.
7. L. Wei, X.L. Pang, C. Liu, and K.W. Gao, *Formation mechanism and protective property of corrosion product scale on X70 steel under supercritical CO_2 environment.* Corrosion Science, 2015. **100**: p. 404-420.
8. Y. Hua, R. Barker, and A. Neville, *Comparison of corrosion behaviour for X-65 carbon steel in supercritical CO_2-saturated water and water-saturated/unsaturated supercritical CO_2* The Journal of Supercritical Fluids, 2015. **97**: p. 224-237.
9. Y. Hua, R. Barker, C. T, M. Ward, and A. Neville, *Relating Iron Carbonate Morphology to Corrosion Characteristics for Water-Saturated Supercritical CO_2 Systems.* The Journal of Supercritical Fluids, 2014. **98**: p. 183-193.
10. Y. Hua, R. Barker, and A. Neville, *Effect of temperautre on the critical water content for general and localised corrosion of X65 carbon steel in the transport of supercritical CO_2.* The International Journal of Greenhouse Gas Control, 2014. **31**: p. 48-60.
11. Y.C. Zhang, X.L. Pang, S.P. Qu, X. Li, and K.W. Gao, *Discussion of the CO_2 corrosion mechanism between low partial pressure and supercritical condition.* Corrosion Science, 2012. **59**: p. 186-197.
12. F. Pessu, R. Barker, and A. Neville, *Understanding Pitting Corrosion Behaviour of X-65 (UNS K03014) Carbon Steel in CO_2 Saturated Environments: The Temperature Effect*, Corrosion, 72(1), pp.78-94.
13. S.N. Esmaeely, S., Y.-S. Choi, D. Young, and S. Nešic, *Effect of calcium on the formation and protectiveness of iron carbonate layer in CO_2 corrosion.* Corrosion, 2013. **69**(9): p. 912-920.

14. S.N. Esmaeely, D. Young, B. Brown, and S. Nešić, *Effect of Incorporation of Calcium into Iron Carbonate Protective Layers in CO_2 Corrosion of Mild Steel.* Corrosion, 2017. **73 (3)**: p. 238-246.
15. D.W.Shannon, *Role of Chemical Components in Geothermal Brine on Corrosion*, in CORROSION 78, 1978: *NACE International.*
16. B. Ingham, M. Ko, N. Laycock, J. Burnell, P. Kappen, J. Kimpton, and D. Williams, *In situ synchrotron X-ray diffraction study of scale formation during CO_2 corrosion of carbon steel in sodium and magnesium chloride solutions.* Corrosion Science, 2012. **56**: p. 96-104.
17. G. Zhao, J. Li, S. Hao, X. Lu, and H. Li, *Effect of Ca^{2+} and Mg^{2+} on CO_2 corrosion behavior of tube steel.* Journal of iron and steel research international, 2005. **12**(1): p. 38-42.
18. C. Ding, K.W. Gao, and C.F. Chen, *Effect of Ca^{2+} on CO_2 corrosion properties of X65 pipeline steel.* International Journal of Minerals, Metallurgy and Materials, 2009. **16**(6): p. 661-666.
19. X. Jiang, Y. Zheng, D. Qu, and W. Ke, *Effect of calcium ions on pitting corrosion and inhibition performance in CO_2 corrosion of N80 steel.* Corrosion science, 2006. **48**(10): p. 3091-3108.
20. C. Ren, X. Wang, L. Liu, H. Yang, and N. Xian, *Lab and field investigations on localized corrosion of casing.* Materials and Corrosion, 2012. **63**(2): p. 168-172.
21. K. Gao, F. Yu, X. Pang, G. Zhang, L. Qiao, W. Chu, and M. Lu, *Mechanical properties of CO_2 corrosion product scales and their relationship to corrosion rates.* Corrosion Science, 2008. **50**(10): p. 2796-2803.
22. L.M. Tavares, E.M. da Costa, J.J. de Oliveira Andrade, R. Hubler, and B. Huet, *Effect of calcium carbonate on low carbon steel corrosion behavior in saline CO_2 high pressure environments.* Applied Surface Science, 2015. **359**: p. 143-152.
23. G. Schmitt, and S. Feinen. *Effect of anions and cations on the pit initiation in CO_2 corrosion of iron and steel*. in *CORROSION 2000*. 2000. NACE International.
24. ASTM, Standard G1-03, Standard practice for preparing, cleaning, and evaluating corrosion test specimens. ASTM International: West Conshohocken, PA, 2003.
25. *MultiScale 7.1 is a commercial software package from Expro Group International Ltd, for more information see: http://multiscale.no/.*
26. Q. Liu, L. Mao, and S. Zhou, *Effects of chloride content on CO_2 corrosion of carbon steel in simulated oil and gas well environments.* Corrosion Science, 2014. **84**: p. 165-171.
27. P.M. Davidson, G.H. Symmes, B.A. Cohen, R.J. Reeder, and D.H. Lindsley, *Synthesis of the new compound $CaFe(CO_3)_2$ and experimental constraints on the (Ca, Fe) CO_3 join.* Geochimica et Cosmochimica Acta, 1993. **57**(23-24): p. 5105-5109.
28. P. Bénézeth, J. Dandurand, and J. Harrichoury, *Solubility product of siderite ($FeCO_3$) as a function of temperature (25–250 C).* Chemical Geology, 2009. **265**(1-2): p. 3-12.
29. G. Dorange, A. Marchand, and M. Le Guyader, *Produit de solubilité de la calcite et constantes de dissociation de $CaHCO_{3+}$ et $CaCO_3$ entre 5 et 75° C.* Revue des sciences de l'eau/Journal of Water Science, 1990. **3**(3): p. 261-275.
30. P. Bénézeth, G.D. Saldi, J.-L. Dandurand, and J. Schott, *Experimental determination of the solubility product of magnesite at 50 to 200 C.* Chemical Geology, 2011. **286**(1-2): p. 21-31.
31. H.A. Alsaiari, N. Zhang, S. Work, A.T. Kan, and M.B. Tomson. *A New Correlation to Predict the Stoichiometry of Mixed Scale: Iron-Calcium Carbonate*. in *SPE International Conference on Oilfield Scale*. 2012. Society of Petroleum Engineers.
32. Y. Hua, R. Jonnalagadda, L. Zhang, A. Neville, and R. Barker, *Assessment of general and localized corrosion behavior of X65 and 13Cr steels in water-saturated supercritical CO_2 environments with SO_2/O_2.* International Journal of Greenhouse Gas Control, 2017. **64**: p. 126-136.
33. S. Mohammed, Y. Hua, R. Barker, and A. Neville, *Investigating pitting in X65 carbon steel using potentiostatic polarisation.* Applied Surface Science, 2017. **423**: p. 25-32.